Morphofunctional changes at the active zone during synaptic vesicle exocytosis

This manuscript ([permalink](#)) was automatically generated from [elatella/deep-prepyto-paper@e0dc886](#) on November 29, 2021.

Authors

- **Amin Khosrozadeh**[*]
  ⓘ [XXXX-XXXX-XXXX-XXXX](#) · ⬡ [ameen-khosrowzadeh](#)
  Institute of Anatomy, University of Bern, Bern, Switzerland; Graduate School for Cellular and Biomedical Sciences, University of Bern · Funded by Grant XXXXXXXX

- **Raphaela Seeger**[*]
  ⓘ [XXXX-XXXX-XXXX-XXXX](#) · ⬡ [elatella](#)
  Institute of Anatomy, University of Bern, Bern, Switzerland; Graduate School for Cellular and Biomedical Sciences, University of Bern

- **Julika Radecke**
  ⓘ [0000-0002-5815-5537](#) · ⬡ [julikaradecke](#)
  Institute of Anatomy, University of Bern, Bern, Switzerland; Department of Neuroscience, Faculty of Health and Medical Science , 2200 Copenhagen N, University of Copenhagen, Copenhagen, Denmark; Diamond Light Source Ltd, Didcot, Oxfordshire, United Kingdom

- **Guillaume Witz**
  ⓘ [0000-0003-1562-4265](#) · ⬡ [guiwitz](#)
  Science IT Service, University of Bern, Bern, Switzerland

- **Vladan Lučić**
  ⓘ [0000-0003-3698-7436](#) · ⬡ [vladanl](#)
  Max-Planck-Institute of Biochemistry, Am Klopferspitz 18, 82152 Martinsried, Germany

- **Jakob B. Sørensen**
  ⓘ [0000-0001-5465-3769](#) · ⬡ [JBSorensen](#)
  Department of Neuroscience, University of Copenhagen, Blegdamsvej 3B, 2200 Copenhagen N, Denmark · Funded by Novo Nordisk Fonden, NNF17OC0028516.; Carlsbergfondet, CF17-0875; Independent Research Fond Denmark, 8020-00228A; Lundbeckfonden, R277-2018-802

- **Benoît Zuber**[✉]
  ⓘ [0000-0001-7725-5579](#) · ⬡ [aseedb](#)
  Institute of Anatomy, University of Bern, Bern, Switzerland · Funded by Swiss National Science Foundation, 179520; ERA-NET NEURON, NEURON-119

✉ Address correspondence to benoit.zuber@ana.unibe.ch and jakobbs@sund.ku.dk.

* These authors contributed equally.

Abstract

The communication between neurons is based on the exocytosis of neurotransmitter filled vesicles. Even small disbalances in this delicate system can result in different disorders. Numerous questions are still unanswered about synaptic vesicle exocytosis regulation as well as about which proteins affect this fundamental process. Hundreds to thousands of vesicles are present at the synapse and most of them are interconnected. There is a number of evidence suggesting that the connectivity between the vesicles influences synaptic vesicle exocytotic activity and that connectivity can be regulated. To address these issues, cryo-electron tomography is a method of choice. Yet inevitable quantitative studies require accurate segmentation of both synaptic vesicles and the interconnecting filaments.

This segmentation process has been widely recognized as a bottleneck by the community. When working with synapses, an incredibly tedious cellular feature to segment are synaptic vesicles. Even though they have a very homogeneous shape and size, which makes it easy to distinguish them from other cellular features, their high occurrence makes their segmentation challenging (one average-sized synapse or synaptosomes can easily contain between 300-500 synaptic vesicles).

Several attempts at utilizing machine learning algorithms to automize the segmentation of synaptic vesicles yielded in unfavorable results. We analyzed these approaches and realized that most algorithms solely worked with the 2D image planes within the tomogram, but didn't tap into their 3D information and therefore increased the weight of the missing wedge.

We designed a framework that consists of two parts: 1) U-Net convolutional network to obtain mask for SVs following by 2) post-processing step which fine-tunes the mask and provides entire 3D-vesicles. A deep-learning model has been trained with manually segmented synaptic vesicles, which have been entirely annotated as 3D objects. By post-processing, we achieved to transfer the vesicle recognition through this pipeline. The evaluation metrics like the DICE value suggest a very high success rate.

Introduction

The rise of machine learning is sweeping the technological landscape. Its use cases are highly diverse and are just starting to reach the scientific community. Especially the graphical deep-learning approaches have been quite popular [1]. But also in the field of cryo electron microscopy has recently recognized the benefits of machine/deep-learning approaches [2].

The method of cryo-electron tomography (ET) utilises a series of tilted two-dimensional (2D) images to reconstruct a three-dimensional (3D) image of the imaged sample [3]. It brings many advantages compared to other cryo-electron microscopy (EM) methods, as it yields images at in situ conditions. Therefore cryo ET can help to reveal the natural cellular environment of protein(-complexes), their function as well as their structure. In order to analyze the cellular context within a tomogram, cellular features are being segmented. Popular programs for manual segementation are IMOD and Amira.
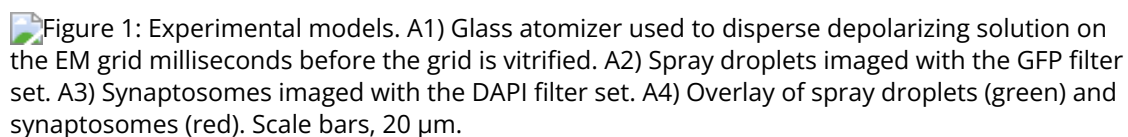
Results

To analyze the morphological changes occurring in the presynpase shortly after stimulation, we pursued a time-resolved cryo-electron tomography approach. A 52-mM KCl containing buffer was sprayed with an atomizer to depolarize synaptosomes and stimulate exocytosis milliseconds before vitrification. The spray droplet size was optimized by cutting a 1-ml pipet tip to a diameter matching

an EM grid (3 mm) and fixed to the atomizer glass outlet to disperse the spray (Figure [1]A1). Furthermore, to achieve a delay of 7 ms between spraying and freezing, the nozzle was set 1-2 mm above the liquid ethane container. This generated many small spray droplets spread throughout the grid (Figure [1]A2-A4). Even if sprayed droplets were well distributed throughout the grid, not all synaptosomes were in contact with exocytosis-triggering KCl solution. Given the very low throughput of cryo-electron tomography, we followed a correlative light and electron microscopy approach. By cryo-fluorescence microscopy, we identified areas where fluorescently labeled synaptosomes and fluorescent spray droplets were colocalized. Additionally, phase contrast imaging enabled quality control of the frozen EM grid with respect to ice contamination and ice cracks, as shown previously [4]. 9 control and 9 stimulated synaptosome tomograms were analyzed. We restricted our analysis to synaptosomes that possessed a smooth PM, free of signs of rupturing and that had a mitochondrion, as we considered these factors essential for synaptosome function.

In addition, we manipulated the electrostatic state of the SNARE complex through a series of point mutations introduced above and grew primary neurons on EM grids [5] (Figure [1]B1-B4). ***More text from Julika and Jakob to describe the procedure here***. Thereby we could image chronically overactive or depressed synapses and relate presynaptic architectural modifications to different functional states.

Figure 1: Experimental models. A1) Glass atomizer used to disperse depolarizing solution on the EM grid milliseconds before the grid is vitrified. A2) Spray droplets imaged with the GFP filter set. A3) Synaptosomes imaged with the DAPI filter set. A4) Overlay of spray droplets (green) and synaptosomes (red). Scale bars, 20 μm.

Figure 1: Experimental models. A1) Glass atomizer used to disperse depolarizing solution on the EM grid milliseconds before the grid is vitrified. A2) Spray droplets imaged with the GFP filter set. A3) Synaptosomes imaged with the DAPI filter set. A4) Overlay of spray droplets (green) and synaptosomes (red). Scale bars, 20 μm.

Increased membrane curvature at the onset of exocytosis

We analyzed the morphology of SVs fusing with the AZ PM. Synaptosomes of a single grid have not all been stimulated for the same duration. Some synaptosomes have been in contact with stimulating solution from the moment the droplet touched the grid, while some others were not at all in contact with the stimulating solution because no droplet landed close enough to them. Importantly, some synaptosomes were located near the point of impact of a droplet, in which case, it took some time for KCl to diffuse until the concentration around these synaptosomes rose sufficiently to trigger exocytosis. Therefore, the time interval between triggering exocytosis and freezing ranged between 0 ms and the interval between spray droplets hitting the grid and freezing, which was comprised between 7 and 35 ms depending on the experiments (Table S2, see also [6]).

Synaptosomes from both control and sprayed grids were thoroughly analyzed for signs of exocytosis, which consisted of morphological changes of the AZ PM and the tethered SV occurring upon stimulation, which are described hereafter. These signs were only detected in synaptosomes from sprayed grids and are presented in the likeliest chronological order. Upon stimulation both the vesicle membrane and the PM were slightly bent towards each other (Figure [2]B1-B3; orange arrows). These structures, which have previously been reported in liposomes but not in synapses, have been referred to as membrane curvature events [7]. Control synaptosomes (i.e. not sprayed) on the other hand, had a straight PM, and no SV membrane was buckled (Figure [2]A). Following membrane bending we observed contacts between vesicles and the PM bilayer where both membranes lose their clear contours (Figure [2]C1 & C2; pink arrows). This was followed by further transitioning states prior to and during pore opening (Figure [2]D-F; blue arrows). In the next observed fusion state, the vesicle was wide open (Figure [2]G), followed by almost completely collapsed vesicles where only a small bump on the PM remained visible (Figure ^{2}H). These structures were not observed in any of the non-sprayed control datasets.

Figure 2: SV exocytosis morphology. Tomographic slice of non-stimulated (A) and stimulated rat synaptosomes (B-H). A) Image of a 2.2-nm thick tomographic slice showing a non-stimulated with SVs at the AZ and a straight PM. B1) Membrane curvature event, 2.2-nm thick tomographic slice. B2) Membrane curvature event, 6.5-nm thick tomographic slice. Orange arrows showing membrane curvature event. C1,C2) Lipid perturbations of PM and SV, 22-nm thick tomographic slices. The space between SV and PM is denser than in the non-stimulated synaptosomes (see pink arrow). D-F) Vesicles with a pore opening that might be on the way to full collapse fusion, 33-nm thick tomographic slice thickness: 22 nm (D), 30.8 (E), 33 nm (F). G) Wide pore opening, most likely on the way to full collapse fusion, 2.2-nm tomographic slice. H) Remaining bump at the end of full collapse fusion, 11-nm thick tomographic slice. Scale bar, 50 nm.

Figure 2: SV exocytosis morphology. Tomographic slice of non-stimulated (A) and stimulated rat synaptosomes (B-H). A) Image of a 2.2-nm thick tomographic slice showing a non-stimulated with SVs at the AZ and a straight PM. B1) Membrane curvature event, 2.2-nm thick tomographic slice. B2) Membrane curvature event, 6.5-nm thick tomographic slice. Orange arrows showing membrane curvature event. C1,C2) Lipid perturbations of PM and SV, 22-nm thick tomographic slices. The space between SV and PM is denser than in the non-stimulated synaptosomes (see pink arrow). D-F) Vesicles with a pore opening that might be on the way to full collapse fusion, 33-nm thick tomographic slice thickness: 22 nm (D), 30.8 (E), 33 nm (F). G) Wide pore opening, most likely on the way to full collapse fusion, 2.2-nm tomographic slice. H) Remaining bump at the end of full collapse fusion, 11-nm thick tomographic slice. Scale bar, 50 nm.

Stimulated synaptosome datasets were divided into early and late fusion stages, respectively, based on the morphology of SV and AZ PM. Synapses showing membrane bending and direct lipid contact between SV and PM without an open pore were classified as early fusion. Those with an open pore or a remaining small bump of a fully collapsed vesicle were classified as late fusion.

Synaptic vesicle distribution is impacted by synaptic activity

Non-stimulated rat synaptosomes as well as WT-SNAP-25 mouse cultured neuron synapses showed typical SV distribution, as observed in previous cryo-ET studies [8]. Vesicle occupancy was 0.08 in the most proximal zone (0-25 nm from the AZ PM), and peaked to 0.17 in 25-50 nm zone. It then dropped to 0.08 in the intermediate zone (50-75 nm) and rose steadily in the more distal zone to reach a plateau of ~0.16 from a distance of 125 nm (Figure ??). These values are for WT-SNAP-25 synapses. The absolute values differ between cultured mouse neurons and rat synaptosomes and but the SV occupancy distribution follows the very same pattern. The difference in absolute values can likely be attributed to the different experimental and animal models used. Sprayed synaptosomes that were showing early signs of exocytosis had a nearly identical SV occupancy pattern as non-sprayed synaptosomes. However, when SV full collapse figures were apparent, SV occupancy in the proximal zone was significantly reduced, whereas SV occupancy further away from the AZ PM was unchanged. This is consistent with some membrane proximal SVs having engaged in exocytosis while none of the recycling and reserve pool SVs have. In order to investigate the consequences of chronic high or low synaptic activity, we investigated the 4E and 4K mutants. In the proximal, intermediate, and the first distal areas (up to approximately 125 nm away from the AZ PM) SVs followed a similar occupancy pattern in the constitutively depressed 4E mutant. This confirmed that the lower activity of the 4E mutant was not due to a lack of SV availability. In the most distal zones, SV occupancy gradually decreased in the mutant *to become significantly different from a distance of XXX nm*. That latter decrease may reflect deleterious effects associated with abnormally low synaptic activity. The 4K mutant displayed significantly decreased SV occupancy in the most proximal area (up to 25 nm), which can be readily attributed to the high probability of spontaneous exocytosis generated by the additional positive charges of the SNARE bundle. From 25 nm to about 125 nm away from the AZ PM the occupancy pattern was similar to the WT situation. Beyond 125 nm occupancy dropped gradually and more steeply than in the case of the 4E mutant. *From a distance of XXX nm, occupancy was significantly lower than in the WT*. This decrease can also be explained by the high exocytosis rate, which leads to a depletion of the reserve pool.

RRP size evolution following stimulation

As stated in the Introduction, SVs that are linked by more than 2 tethers to the AZ PM have been shown to belong to the RRP. We investigated the tethering state of proximal SVs (i.e. those SVs within 45 nm of the AZ PM) prior and following stimulation in synaptosomes. In non-sprayed synaptosomes, 59% of the proximal vesicles were tethered, which is in agreement with previous results [8]. Interestingly, in the early fusion group the fraction of tethered proximal vesicles significantly increased to 80% (P<0.05, χ^2 test; Figure ??).

FIGURE TETHERS : one panel for fraction of proximal vesicles that are tethered in synaptosomes. One panel for the same but in neurons. Two panels for fraction of proximal vesicles in RRP (one for synaptosomes, one for neurons). Two panels for number of tethers per proximal sv (one for synaptosomes, one for neurons). two panels for swarm plot of vesicle distance.

In the late fusion group, however, 47% of the proximal vesicles were tethered, which is not significantly different to the non sprayed group. We then analyzed whether the decreased occupancy in the late fusion group was associated with a decreased number of RRP SVs. In resting, non-sprayed synapses about 11% of the proximal SVs resided in the RRP. This agrees with typical RRP size estimates based on electrophysiological measurements. Surprisingly, the fraction of proximal vesicles belonging to the RRP drastically increased to 36% in the early fusion group (P<0.001, χ^2 test; Figure ??). The fraction returned to the initial value of 11% in the late fusion group. This 3-fold increase over the baseline RRP SVs in the early fusion group suggests that upon stimulation some proximal SVs very rapidly enter the RRP and become primed for exocytosis. Furthermore, the lower proximal vesicle occupancy in the late fusion group indicates that under our stimulation conditions, replenishing vesicles to the proximal zone is slower than their release.

The situation in the WT-SNAP-25 neurons was similar to unstimulated synaptosomes. 53% of the all proximal SVs were tethered and 14% of all proximal SVs belonged to the RRP. WT proximal SVs The corresponding values for the 4E mutants were not significantly different. However, In all 4K mutant datasets there was not a single SV that was part of the RRP. Consistently, the number of tethers per proximal SV was significantly lower in the 4K mutant than in the WT. These results are in line with physiological measurements that have shown that the RRP is depleted in the chronically spontaneously active 4K mutant, and they provide additional evidence that RRP-vesicles have at least 3 tethers. [5].
Furthermore, the average distance between proximal SVs and the AZ PM is significantly higher in the 4K mutant than in the WT, suggesting that vesicles coming into close contact with the AZ PM undergo spontaneous exocytosis, and are depleted.

Synaptic activity modifies inter-SV connectivity

The majority of SV are connected to other SVs through so-called connectors [8,9]. Connector function and composition is not clear yet. It is generally assumed that synapsin is involved in connector formation and may be one of its components. It has been suggested that connectors reduce SV mobility and maintain a local high SV concentration in the presynpase. The connectivity level of an individual SV might be one of the factors defining the pool to which the SV belongs. To shed some light on the role of connectors we analyzed SV connectivity in our datasets. We focused most of *(all?)* our analysis to the SVs located at distance of the AZ PM lower than 250 nm. Furthermore, we defined 4 distance groups: proximal (0-45 nm), intermediate (45-75 nm), distal 1 (75-150 nm), distal 2 (150-250 nm), as in previous studies [8,10]. We first analyzed synaptosomes.

FIGURE CONNECTORS. two panels for fraction of proximal vesicles that are connected as a function of distance (distance groups; one for synaptosomes, one for snap-25). two panels for fraction of proximal vesicles that are connected as a function of RRP.

In non-sprayed synaptosomes datasets, approximately 80% of the proximal and intermediate SVs were connected to other vesicles. In distal 1 and 2 regions, this value rose to 85 and 93%, respectively. sprayed, early and late fusion groups showed a similar pattern with one interesting exception. Proximal SV connectivity dropped to 58% in the late fusion group (P<0.05, χ^2 test; Figure [**figure:connectors?**]). This decrease originates from SVs that are not in the RRP of which only 52.9% of the vesicles were connected as opposed to 77.5% before stimulation (P<0.01, χ^2 test; Figure ??). These results are consistent with an observed decrease in the number of connectors per proximal SV that are not part of the RRP, from 1.81±0.18 connector per SV in the non sprayed group to 0.85±0.16 in the late fusion group (P<0.01, K-W test) (Figure ??). Connectors between proximal vesicles (Figure ??) were found to remain between fusing vesicles (Figure ?? and Supplementary movie S1). We hypothesize that given the free space made in the proximal region after some SVs have fused, non-connected vesicles from the intermediate region diffuse to the proximal zone and become tethered to the AZ PM. Our data suggest that establishing connectivity is a slower process than tethering.

We then analyzed SNAP-25 mutants. Similarly to non-sprayed synaptosome, the fraction of connected SVs was significantly higher in the distal 2 group, albeit the absolute values were overall lower than in synaptosomes. SNAP-25-WT synapses showed a higher level of connectivity in the distal group. The fraction of connected SVs in both distal groups was significantly lower in the 4E mutant than in the WT. In the case of the 4K mutant, the difference was significant in the distal 2 group. Consistently, a significantly lower number of connectors per SV was observed in both distal groups of the 4E and the 4K mutants with respect to the WT. Additionally, the 4E mutant had significantly less connectors per proximal SV than the WT, whereas the 4K mutant had significantly less connectors per intermediate SV than the WT. These results indicate that prolonged abnormal exocytotic activity is correlated with changes in intervesicular connectivity.

Discussion

Materials and methods

Constructs and viruses

SNAP-25B was N-terminally fused to GFP and cloned into a pLenti construct with a CMV promoter [11]. Mutations were made using the QuikChange II XL kit (Agilent). The mutations were verified by sequencing and have been published before [5]. The preparation of lentiviral particles followed standard protocols.

Animals

Synaptosomes were prepared from adult male or female Wistar rat obtained from the central animal facilities of the Department of Biomedical Research of the University of Bern. Adult male or female Wistar rats at an age of 6-8 weeks were slightly stunned by CO_2 and quickly decapitated with a guillotine. The procedures used were in accordance with the Swiss Veterinary Law guidelines. Heterozygous SNAP-25 KO C57/Bl6-mice were routinely backcrossed to Bl6 to generate new heterozygotes. The strain was kept in the heterozygous condition and timed heterozygous crosses and caesarean section were used to recover knockout embryos at embryonic day 18 (E18). Pregnant females were killed by cervical dislocation; embryos of either sex were collected and killed by decapitation. Permission to keep and breed SNAP-25 mice was obtained from the Danish Animal Experiments Inspectorate and followed institutional guidelines as overseen by the Institutional Animal Care and Use Committee (IACUC). CD1 outbred mice were used to create astrocytic cultures. Newborns (P0-P2) of either sex were used. Pups were killed by decapitation.

Synaptosome preparation

Rat synaptosomes were prepared as previously described [12], with some modifications. The cerebral cortex and the hippocampi were removed in sucrose buffer (SEH: 0.32 M sucrose, 1 mM EDTA, 10 mM HEPES; HEPES, #H4034, Sigma-Aldrich Corporate Offices. St. Louis, MO, USA) on ice. Homogenization of the tissue was done in SEH with a Potter-Elvehjem grinder (#358011, Wheaton. Millville, New Jersey, USA), four strokes at the bottom and 6 from top to bottom were applied to the tissue at a speed of 800 turns/min as described in [12]. The whole process from decapitation to homogenization was done within 2-3 min, to obtain functional synaptosomes. Homogenized tissue was then centrifuged at 1000 g for 10 min at 4°C to remove meninges and blood vessels. The resulting supernatant containing synaptosomes, but also gliosomes and mitochondria was then added to a discontinuous, isoosmotic Percoll (#P1644, Sigma) gradient with 5%, 10% and 23% in 0.32 M sucrose, 1 mM EDTA in centrifuge tubes (#344060, Beckman Coulter). The samples were spun in an ultracentrifuge (rotor: SW 40 Ti; Beckman Coulter. Nyon, Switzerland) at 16400 rpm for 12 min at 4°C. The layer with the highest amount of functional synaptosomes was between 10-23 % [12]. The layer was carefully taken out and diluted 1:10 in HEPES buffered medium (HBM; 140 mM NaCl, 5 mM KCl, 5 mM $NaHCO_3$, 1.2 mM Na_2HPO_4, 1 mM $MgCl_2$, 10 mM Glucose, 20 mM HEPES). The obtained solution was further spun with an ultracentrifuge (rotor 45 Ti; Beckman Coulter) at 11200 rpm for 20 min at 4°C. The pellet was carefully and quickly aspirated with a Pasteur pipette to avoid mixture with the solution and then diluted in HBM.

Preparation of astrocytic and neuronal culture

The procedure has been published before [13]. Glial cells were ready to be used after 10 days. once they were triturated and counted with a Buerker chamber, 100,000 cells/ml were plated onto untreated 12 well plates containing 10% DMEM. Astrocytes were isolated from CD1 outbred mice (P0-P2). Pups were killed by decapitation and heads were placed in HBSS-HEPES medium (HBSS supplemented with 1 M HEPES). The cortices were isolated from the brains and the meninges were removed (dura, pia and arachnoid mater). The cortices were chopped into smaller fragments and transferred to a tube containing 0.25% trypsin dissolved in Dulbecco's MEM (DMEM)supplemented with 10% foetal calf serum, 20000 IU penicillin, 20 mg streptomycin and 1% MEM non-essential amino acids. Fragments were incubated for 15 min at 37°C. Subsequently, inactivation medium (12.5 mg albumin + 12.5 mg trypsin-inhibitor in 10% DMEM) was added and the tissue washed with HBSS-HEPES. Tissue was triturated until a smooth cloudy suspension appeared. Cells were plated in 80 cm^2 flasks with pre-warmed DMEM, one hemisphere per flask, and stored at 37°C with 5% CO_2. Glial cells were ready to be used after 10 days. Glial cells were washed with pre-warmed HBSS-HEPES. Trypsin was added and the flasks were incubated at 37°C for 10 min. Cells were triturated and counted with a Buerker chamber before plating 100,000 cells/ml on untreated 12-well plates containing DMEM. After 2 days, neurons were plated.

Hippocampal neurons were isolated from either E18 SNAP-25 KO. The SNAP-25 KO pups were obtained by pairing two heterozygote animals, and the embryos were recovered at E18 by caesarean section. Pups were selected based on the absence of motion after tactile stimulation and bloated neck [14]; the genotype was confirmed by PCR in all cases. The pups were killed by decapitation and heads were put in HBSS-HEPES medium. The cortices were isolated from the brains and the meninges were removed. The hippocampi were cut from the cortices before being transferred to a tube containing 0.25% trypsin dissolved in HBSS-HEPES solution. Fragments were incubated for 20 min at 37°C. Afterwards, the tissue was washed with HBSS-HEPES. The hippocampi were triturated and the cell count was determined with a Buerker chamber. 20 µl of solution containing 250,000 cells/ml were plated onto the flame sterilized gold R2/2 or R2/1 EM grids as previously described in [13]. Following a 30 min incubation at 37°C, the grid was transferred into the 12 well plate containing the astrocytes and medium was replaced with NB medium (Neurobasal with 2% B-27, 1 M HEPES, 0.26% lutamax, 14.3 mM β-mercaptoethanol, 20000 IU penicillin, 20 mg streptomycin) for the E18 pups or NB-A

medium (Neurobasal-A with 2% B-27, 1% Glutamax , 20000 IU Penicillin, 20 mg Streptomycin) for the P0-P1. Between 4 h and 1 day later, lentiviral particles carrying either SNAP-25-WT, SNAP-25-4E, or SNAP-25-4K constructs were added to the culture. The cultures were incubated for 12 to 14 days before being plunge frozen.

Plunge freezing and spray-mixing

Rat synaptosomes were prepared for plunge freezing and spray-mixing as follows. The following steps from incubation to plunge freezing were all done at room temperature (RT), equivalent to 23-25°C. The synaptosomal solution was incubated with calcein blue AM (#C1429, Molecular Probes-Thermo Fisher Scientific. Waltham, MA, USA) 30 min prior to plunge freezing to visualize the cytosol of functional – esterase containing – cellular compartments such as synaptosomes. Additionally, 1.3 mM $CaCl_2$ and 10 nm gold fiducials were added (gold fiducials, #s10110/8. AURION Immuno Gold Reagents & Accessories. Wageningen, The Netherlands). $CaCl_2$ is necessary to trigger exocytosis and gold fiducials are important to align the acquired tilt series for tomogram reconstruction. The sprayed solution contained 1 mM $CaCl_2$ and 52 mM KCl in HBM to depolarize synaptosomes and trigger exocytosis. It also contained fluorescein (#46955, Sigma) to trace the spray droplets on the EM grid in cryo-FM. The synaptosomal solution was applied to a 200-mesh lacey finder carbon film grid (#AGS166-H2. Agar Scientific. Elektron Technology UK Ltd. Stansted, UK). Excess liquid on the grid was removed by blotting with a filter paper and the grid was immediately plunge frozen in liquid ethane with a homebuilt plunge freezer and was sprayed on the fly. The plunge freezer and the spraying device (atomizer) were computer controlled with a LabView script (National Instruments Corporation. Mopac Expwy Austin, TX, USA). The spraying device was set similarly to the device in [15]. Nitrogen gas pressure necessary to drive spraying was set to 2.5 bar. The grid was set to pass in front of the spray nozzle at a distance of 3-4 mm. The plunge freezer was accelerated to 0.75 m/s and the minimum spray delay was ~7 ms (Table S3). The atomizer sprays scattered droplets of various size on the EM grid. During the time lapse between spraying and freezing the content of the droplets spreads by diffusion. KCl diffuses approximately 4x faster than fluorescein. Cryo-ET imaging was done within the diffusion distance of KCl but outside of the visible spray droplet because the center of the spray droplet would usually be too thick for imaging. This reduces the effective stimulation duration to anything between 0 ms and less than the given spray-freeze delay. Moreover, through diffusion, KCl concentration rapidly rises and then decreases. Hence synaptosomes are not permanently depolarized.

After 12 to 14 days of incubation grids with mouse neurons were plunge frozen with a Vitrobot (Thermofisher Scientific, Mark IV) with a blot time of 3 s and a blot force of -10. Wait time and drain time were not used. Humidity was set to 100% at 4°C. 4 µl undiluted 10 nm BSA gold tracer (Aurion) was added directly onto the grid prior to plunge freezing.

Cryo-fluorescence microscopy

After plunge freezing, rat synaptsome samples were imaged at the fluorescent microscope under cryo conditions, with a Zeiss Axio Scope.A1, equipped with an AxioCam MRm camera (Carl Zeiss AG, Germany), and a fluorescence lamp (HXP 120 C). The correlative microscopy stage (#CMS196, Linkam Scientific Instruments, UK) was cooled down to -190°C by liquid nitrogen and the frozen EM grid was placed into the chamber of the cryostage on a bridge that was not submerged in liquid nitrogen and was close to the objective, where the temperature was around -150°C. The filter set used for imaging fluorescein was #38 (#000000-1031-346, Zeiss) (BP 470/40, FT 495, BP 525/50; corresponds to GFP) and the one for calcein blue AM was #49 (#488049-9901-000, Zeiss) (G 365, FT 395, BP 445/50; corresponds to DAPI). The objective used was either a 10x (#420941-9911, NA = 0.25 Ph1, Zeiss) or a 50x (#422472-9900, NA = 0.55 Dic, Zeiss), the acquisition software used was AxioVision (AxioVs40x64 V 4.8.3.0, Zeiss) and the processing software was ZEN lite (Zeiss).

Cryo-electron microscopy

Following cryo-FM, the rat synaptosome grids were mounted in a cryo-holder (Gatan, Pleasonton, CA, USA) and transferred to a Tecnai F20 (FEI, Eindhoven, The Netherlands) which was set to low dose conditions, operated at 200 kV, and equipped with a field emission gun. Images were recorded with a 2k x 2k CCD camera (Gatan) mounted after a GIF Tridiem post-column filter (Gatan) operated in zero-loss mode. The sample was kept at about -180°C. Tilt series were acquired using SerialEM [16] for automated acquisition recorded typically from -50° to 50° with a 2° angular increment and an unbinned pixel size of 0.75 or 1.2 nm. Due to sample thickness (400-700 nm), tomograms were usually not recorded with higher tilt angles. Defocus was set between -8 to -12 μm and the total electron dose used was about 80-100 e$^-$/Å^2. Some tomograms were acquired at a Titan Krios equipped with a K2 direct electron detector (Gatan) without energy filter. The K2 camera was operated in superresolution counting mode and between 8-40 frames per tilt angle were taken. Tilt series were acquired using the Latitude software (Gatan) for automated acquisition recorded typically from -60° to 60° with a 2° angular increment and an unbinned pixel size of 0.6 nm. Defocus was set between -8 to -12 μm and the total electron dose used was about 80-100 e$^-$/Å^2. Prior to image processing the frames at each tilt angle, frames were aligned and averaged in 2dx MC_Automator [17] with motioncor [18]. 3D reconstruction was done in IMOD [19]. The alignments were done using the automated fiducial tracking function and the 3D reconstructions were done using the weighted back projection followed by a nonlinear anisotropic diffusion (NAD) filtering. Following tomogram reconstruction only synaptosomes that fulfilled the following criteria were used: 1) even and non-broken PM, 2) synaptic cleft still attached to the presynapse, 3) spherical vesicles, and 4) a mitochondrion in the presynapse necessary to cover the energy demands of the synapse. These criteria indicate that the synaptosome is functional [20].

Cultured mouse neurons tilt series were acquired at a Titan Krios, equipped with a Falcon 3 direct electron detector (Thermofisher Scientific) without energy filter. The Falcon camera was operated in linear mode. Tilt series were acquired using the TEM Tomography software (TFS) for automated acquisition recorded typically from -60° to 60° with a 2° angular increment and an unbinned pixel size of 0.37 nm. Defocus was set between -6 to -10 μm and the total electron dose used was about 80-100 e$^-$/Å^2. Tomogram reconstruction was done as for synaptosome datasets.

Manual and automatic segmentation procedures

Manual segmentation of SVs, mitochondria, and the active zone PM was done in IMOD (Figure S4A&B). The boundary marked the region to be analyzed by Pyto [21]. The analysis by Pyto was essentially the same as described previously [8] [21]. In short, the segmented area is divided in 1 voxel thick layers parallel to the active zone for distance calculations. A hierarchical connectivity segmentation detects densities interconnecting vesicles (so called connectors) and densities connecting vesicles to the active zone PM (so called tethers) (Figure S4C). Distance calculations are done with the center of the vesicle. Mainly default settings were used. The segmentation procedure is conservative and tends to miss some tethers and connectors because of noise. Consequently, the numbers of tethers and connectors should not be considered as absolute values but rather to compare experimental groups. All tomograms analyzed by Pyto were obtained on the same microscope with the same tilt range. The margin of error for false negatives and positives was found to be less than 10% by comparison with ground truth [21]. As it was done before, an upper limit was set between 2100 and 3200 nm3 on segment volume. The tomograms that were used for this analysis were binned by a factor of 2 to 3, resulting in voxel sizes between 2.1 and 2.4 nm. Tether and connector length were calculated using the midpoint method [21]. From the stimulated synaptosomes only those that showed visible signs of exocytosis where used for analysis in Pyto.

Data analysis

If not stated otherwise data in the text are described as mean ± standard error to the mean (SEM). Wherever possible, data were presented as box plots with the following settings: orange bar, median; box extremities, lower and upper quartiles; whiskers extend up to 1.5 x interquartile range; dots, outliers. We used the same statistical tests as in [8,10]. For normal distributed data, the Student's t-test was used. **remove the following sentence if necessary** For data deviating from the normal distribution, the Kruskal-Wallis (K-W) test was used. In addition, for data that required to be split into discrete bins (e.g. fraction of connected vesicles by distance to active zone), the $\chi 2$ test was used. To calculate the correlation coefficient for paired samples (such as vesicle distance to active zone and number of tethers), Spearman's rank correlation was used (ρ-test). The confidence values were calculated using two-tailed tests and were indicated in the graphs by , *P<0.05;* **, P<0.01;** , P<0.001. We did not apply statistical methods to predetermine sample size but similar sample sizes as previously reported have been used [8]. It was not necessary to apply randomization.

References

1. **Machine Learning in Medicine**
   Alvin Rajkomar, Jeffrey Dean, Isaac Kohane
   New England Journal of Medicine (2019-04-04) https://doi.org/gfzk8r
   DOI: 10.1056/nejmra1814259 · PMID: 30943338

2. **Application of machine learning techniques to electron microscopic/spectroscopic image data analysis**
   Shunsuke Muto, Motoki Shiga
   Microscopy (2020-04) https://doi.org/ggckm4
   DOI: 10.1093/jmicro/dfz036 · PMID: 31682260 · PMCID: PMC7141894

3. **Current data processing strategies for cryo-electron tomography and subtomogram averaging**
   Euan Pyle, Giulia Zanetti
   Biochemical Journal (2021-05-28) https://doi.org/gkqqv6
   DOI: 10.1042/bcj20200715 · PMID: 34003255 · PMCID: PMC8133831

4. **Correlative microscopy: Bridging the gap between fluorescence light microscopy and cryo-electron tomography**
   Anna Sartori, Rudolf Gatz, Florian Beck, Alexander Rigort, Wolfgang Baumeister, Juergen M Plitzko
   Journal of Structural Biology (2007-11) https://doi.org/cp5krz
   DOI: 10.1016/j.jsb.2007.07.011 · PMID: 17884579

5. **An Electrostatic Energy Barrier for SNARE-Dependent Spontaneous and Evoked Synaptic Transmission**
   Marvin Ruiter, Anna Kádková, Andrea Scheutzow, Jörg Malsam, Thomas H Söllner, Jakob B Sørensen
   Cell Reports (2019-02) https://doi.org/gfv5gd
   DOI: 10.1016/j.celrep.2019.01.103 · PMID: 30811985

6. **Analysis of transient structures by cryo-microscopy combined with rapid mixing of spray droplets.**
   J Berriman, N Unwin
   Ultramicroscopy (1994-12) https://www.ncbi.nlm.nih.gov/pubmed/7831735
   DOI: 10.1016/0304-3991(94)90012-4 · PMID: 7831735

7. **Membrane Curvature in Synaptic Vesicle Fusion and Beyond**
   Harvey T McMahon, Michael M Kozlov, Sascha Martens
   Cell (2010-03) https://doi.org/d3gmvv
   DOI: 10.1016/j.cell.2010.02.017 · PMID: 20211126

8. **Quantitative analysis of the native presynaptic cytomatrix by cryoelectron tomography**
   Rubén Fernández-Busnadiego, Benoît Zuber, Ulrike Elisabeth Maurer, Marek Cyrklaff, Wolfgang Baumeister, Vladan Lučić
   Journal of Cell Biology (2010-01-11) https://doi.org/b9c26b
   DOI: 10.1083/jcb.200908082 · PMID: 20065095 · PMCID: PMC2812849

9. **Molecular architecture of the presynaptic terminal**
   Benoît Zuber, Vladan Lučić
   Current Opinion in Structural Biology (2019-02) https://doi.org/gk8gpd
   DOI: 10.1016/j.sbi.2019.01.008 · PMID: 30925443

10. **Cryo–electron tomography reveals a critical role of RIM1α in synaptic vesicle tethering**
    Rubén Fernández-Busnadiego, Shoh Asano, Ana-Maria Oprisoreanu, Eri Sakata, Michael Doengi, Zdravko Kochovski, Magdalena Zürner, Valentin Stein, Susanne Schoch, Wolfgang Baumeister, Vladan Lučić
    Journal of Cell Biology (2013-05-27) https://doi.org/f4x2mj
    DOI: 10.1083/jcb.201206063 · PMID: 23712261 · PMCID: PMC3664715

11. **Differential Abilities of SNAP-25 Homologs to Support Neuronal Function**
    I Delgado-Martinez, RB Nehring, JB Sorensen
    Journal of Neuroscience (2007-08-29) https://doi.org/d7mhxn
    DOI: 10.1523/jneurosci.5092-06.2007 · PMID: 17728451 · PMCID: PMC6673127

12. **A rapid Percoll gradient procedure for preparation of synaptosomes**
    Peter R Dunkley, Paula E Jarvie, Phillip J Robinson
    Nature Protocols (2008-10-16) https://doi.org/b7zwh8
    DOI: 10.1038/nprot.2008.171 · PMID: 18927557

13. **Preparation of Primary Neurons for Visualizing Neurites in a Frozen-hydrated State Using Cryo-Electron Tomography**
    Sarah H Shahmoradian, Mauricio R Galiano, Chengbiao Wu, Shurui Chen, Matthew N Rasband, William C Mobley, Wah Chiu
    Journal of Visualized Experiments (2014-02-12) https://doi.org/gmh9w3
    DOI: 10.3791/50783 · PMID: 24561719 · PMCID: PMC4089403

14. **Genetic ablation of the t-SNARE SNAP-25 distinguishes mechanisms of neuroexocytosis**
    Philip Washbourne, Peter M Thompson, Mario Carta, Edmar T Costa, James R Mathews, Guillermina Lopez-Benditó, Zoltán Molnár, Mark W Becher, CFernando Valenzuela, LDonald Partridge, Michael C Wilson
    Nature Neuroscience (2001-12-19) https://doi.org/fbmxgc
    DOI: 10.1038/nn783 · PMID: 11753414

15. **Analysis of transient structures by cryo-microscopy combined with rapid mixing of spray droplets**
    John Berriman, Nigel Unwin
    Ultramicroscopy (1994-12) https://doi.org/ctwp5j
    DOI: 10.1016/0304-3991(94)90012-4

16. **Automated electron microscope tomography using robust prediction of specimen movements**
    David N Mastronarde
    Journal of Structural Biology (2005-10) https://doi.org/ff7gzx
    DOI: 10.1016/j.jsb.2005.07.007 · PMID: 16182563

17. **2dx_automator: Implementation of a semiautomatic high-throughput high-resolution cryo-electron crystallography pipeline**
    Sebastian Scherer, Julia Kowal, Mohamed Chami, Venkata Dandey, Marcel Arheit, Philippe Ringler, Henning Stahlberg
    Journal of Structural Biology (2014-05) https://doi.org/f522h3
    DOI: 10.1016/j.jsb.2014.03.016 · PMID: 24680783

18. **Electron counting and beam-induced motion correction enable near-atomic-resolution single-particle cryo-EM**
    Xueming Li, Paul Mooney, Shawn Zheng, Christopher R Booth, Michael B Braunfeld, Sander Gubbens, David A Agard, Yifan Cheng
    Nature Methods (2013-05-05) https://doi.org/f4zpjf

DOI: [10.1038/nmeth.2472](#) · PMID: [23644547](#) · PMCID: [PMC3684049](#)

19. **Computer Visualization of Three-Dimensional Image Data Using IMOD**
James R Kremer, David N Mastronarde, JRichard McIntosh
Journal of Structural Biology (1996-01) https://doi.org/d9nfzw
DOI: [10.1006/jsbi.1996.0013](#) · PMID: [8742726](#)

20. **A rapid Percoll gradient procedure for isolation of synaptosomes directly from an S1 fraction: viability of subcellular fractions**
Steven M Harrison, Paula E Jarvie, Peter R Dunkley
Brain Research (1988-02) https://doi.org/b5tzcr
DOI: [10.1016/0006-8993(88)91384-4](#)

21. **Hierarchical detection and analysis of macromolecular complexes in cryo-electron tomograms using Pyto software**
Vladan Lučić, Rubén Fernández-Busnadiego, Ulrike Laugks, Wolfgang Baumeister
Journal of Structural Biology (2016-12) https://doi.org/f9d5t2
DOI: [10.1016/j.jsb.2016.10.004](#) · PMID: [27742578](#)